# First Results of the THEMIS Search Coil Magnetometers

O. Le Contel  $\cdot$  A. Roux  $\cdot$  P. Robert  $\cdot$  C. Coillot  $\cdot$  A. Bouabdellah  $\cdot$  B. de la Porte  $\cdot$  D. Alison  $\cdot$  S. Ruocco  $\cdot$  V. Angelopoulos  $\cdot$  K. Bromund  $\cdot$  C.C. Chaston  $\cdot$  C. Cully  $\cdot$  H.U. Auster  $\cdot$  K.H. Glassmeier  $\cdot$  W. Baumjohann  $\cdot$  C.W. Carlson  $\cdot$  J.P. McFadden  $\cdot$  D. Larson

Received: 11 February 2008 / Accepted: 21 April 2008 / Published online: 4 June 2008 © Springer Science+Business Media B.V. 2008

**Abstract** We present the first data from the THEMIS Search Coil Magnetometers (SCM), taken between March and June 2007 while the THEMIS constellation apogee moved from the duskside toward the dawnside. Data reduction, especially the SCM calibration method and spurious noise reduction process, is described. The signatures of magnetic fluctuations in key magnetospheric regions such as the bow shock, the magnetopause and the magnetotail during a substorm, are described. We also discuss the role that magnetic fluctuations could play in plasma transport, acceleration and heating.

O. Le Contel (🖾) · A. Roux · P. Robert · C. Coillot · A. Bouabdellah · B. de la Porte · D. Alison ·

S Ruocco

Centre d'étude des Environnements Terrestre et Planétaires (CETP), 10-12 avenue de l'Europe, 78140

Vélizy, France

e-mail: olivier.lecontel@cetp.ipsl.fr

V. Angelopoulos

IGPP/UCLA, Los Angeles, CA 90095, USA

K Bromund

SP Systems, Inc. on contract to NASA/GSFC, Space Weather Laboratory, Code 674, Greenbelt, MD, USA

C.C. Chaston

Space Sciences Laboratory, University of California, Berkeley, CA, USA

C. Cully

Laboratory for Atmospheric and Space Physics, University of Colorado, Boulder, CO, USA

H.U. Auster · K.H. Glassmeier

Institut für Geophysik und extraterrestrische Physik der Technischen Universität Braunschweig, 38106 Braunschweig, Germany

W. Baumjohann

Space Research Institute, Austrian Academy of Sciences, Graz, Austria

C.W. Carlson · J.P. McFadden · D. Larson

Space Sciences Laboratory, University of California, Berkeley, CA, USA



**Keywords** THEMIS  $\cdot$  Solar wind  $\cdot$  Shock  $\cdot$  Magnetosheath  $\cdot$  Flux transfer event  $\cdot$  Magnetopause  $\cdot$  Substorm  $\cdot$  Search-coil  $\cdot$  ULF/ELF magnetic waves

#### 1 Introduction

The identification of the instability leading to substorm breakup and expansion is a key issue for magnetospheric physics and beyond. Indeed similar explosive processes are known to occur in other astrophysical contexts, such as the solar corona, and in laboratory machines designed for controlled fusion. In all cases the accumulated magnetic energy is released explosively, thereby leading to fast changes in the magnetic configuration and particle acceleration. These plasmas being hot and dilute, binary collisions are rare and cannot supply the dissipation needed for the development of instabilities that can break the magnetic configuration, such as the collisionless tearing instability. Kinetic effects, in particular associated with the development of waves, are expected to take over the role that binary collisions cannot fulfill.

Together with the Electric field Instrument (EFI) (Bonnell et al. 2008), the THEMIS Search Coil Magnetometer (SCM) (Roux et al. 2008) will be used to identify the possible role of waves at substorm breakup and expansion phase. It will also allow the remote tracking of the motion of active regions, via ducted waves.

The association between substorm onset and intense emissions of ULF/ELF/VLF waves has been known for quite a long time (Gendrin 1970; Russel 1972; Gurnett et al. 1976). Later, the search coils magnetometers onboard the geostationary European satellite GEOS-2, launched in 1978, detected magnetic impulsive signals in the range 0.5–11.5 Hz (ULF) at substorm breakup (Robert et al. 1984), characterized by particle injection and changes from a tail-like to a more dipolar magnetic configuration. Robert et al. interpreted the Short Irregular Pulsations (SIPs) observed at breakup as the signatures of small scale field aligned current structures passing by the spacecraft (Robert et al. 1984). Due to their non-steadiness, these structures can also be interpreted as kinetic Alfvén waves in the proton gyrofrequency (0.1–1 Hz) range (Perraut et al. 1993). Kremser et al. showed that electron parallel acceleration takes place inside these structures (Kremser et al. 1988).

On the basis of AMPTE/CCE data ( $X_{GSM} \simeq -8.8~R_E$ ), Lui et al. suggested that the cross field current driven instability triggers substorm onset (Lui et al. 1991, 1996). Farther in the magnetotail ( $X_{GSM} \simeq -15.2~R_E$ ), observations from the Japanese Geotail satellite give evidence for the existence of electromagnetic waves in the lower hybrid frequency range during a small substorm (Shinohara et al. 1998). Yet the authors concluded that wave energy is too small to supply enough dissipation, via anomalous resistivity, to allow a resistive-mode instability to develop. On the theoretical side, Cheng and Lui proposed another solution to resolve the substorm onset enigma; they suggested that the coupling between high frequency (cross tail current instability) and low frequency (ballooning mode) electromagnetic fluctuations accounts for the fast occurrence of the breakup onset (Cheng and Lui 1998). As the Geotail apogee moved closer to the earth ( $X_{GSM} \simeq -10$  to  $-13~R_E$ ), magnetic fluctuations were also observed during substorm in the proton gyrofrequency (0.1–1 Hz) range as well as in the lower hybrid frequency range (5–16 Hz). However, according to Sigsbee et al. these fluctuations reach their maximum amplitude after onset and could not therefore be considered as a substorm trigger (Sigsbee et al. 2001).

Further analysis of GEOS-2 data (at the geostationary orbit) suggested that substorm onset and impulsive plasma transport is controlled by a micro-instability with frequencies around the proton gyrofrequency such as a parallel current instability (Perraut et al. 2000a,



2000b; Le Contel et al. 2001a, 2001b). The regular occurrence at different radial distances (at the geostationary orbit with GEOS-2, at 10  $R_E$  with Geotail and 20  $R_E$  with Cluster) of wave activity around the proton gyrofrequency at substorm onset was also noted by Le Contel et al. (2002). Yet more recent analysis of Geotail observations in the near-earth plasma sheet ( $X_{GSM} \simeq -8.3 R_E$ ) gave evidence for large amplitude wave emissions (5–15 nT s<sup>-1</sup>) in the lower hybrid frequency range (5–20 Hz), just prior to the dipolarization (Shiokawa et al. 2005). Thus the identification of the intense waves that develop at substorm onset, and the elucidation of their potential role at triggering breakup, is still a matter of debate.

In this context the determination of the radial distribution of wave characteristics is an important issue that should be resolved thanks to THEMIS wave instrumentation. The THEMIS orbit is well suited to achieve this goal (Angelopoulos et al. 2008; Sibeck and Angelopoulos 2008a), but the full characterization of the waves is made difficult by the rapid changes of the magnetic configuration during substorm and by the strong inhomogeneity of the medium. In order to avoid adding confusion in the debate it would be wise to use the same parameter, namely the amplitude B of the waveform, rather than its derivative ( $\omega B$ ). Indeed the use of the derivative can give the false impression that amplitudes are larger at larger frequencies.

At higher frequencies, whistler waves were identified in the magnetotail and proposed as a way to monitor energetic electrons and processes of reconnection (Zhang et al. 1999). More recently, Cluster observations from the STAFF instrument (Cornilleau-Wehrlin et al. 2003) gave evidence for very large amplitude ( $\simeq 1$  nT) waves in the whistler mode range ( $f_{ci} < f < f_{ce}$ ), emitted in the magnetotail during substorms (Le Contel et al. 2006). These intense emissions last only a few seconds and are associated with very thin current sheets ( $\leq \rho_i$ , the proton Larmor radius). They occur in conjunction with accelerated electrons. Whistler mode waves are expected to be produced in some of the magnetic reconnection theories (Mandt et al. 1994). Yet, at present time, it is unclear whether they are a by-product of reconnection or whether they effectively play a crucial role as a trigger of the substorm process. Further studies are therefore needed in order to clarify the role of these different kinds of wave during various substorm phases.

Substorms are not the only space physics process for which waves could play a crucial role. Magnetic reconnection and plasma transport at the magnetopause can be modeled as a global process controlled by the level of ULF wave activity (see for instance Rezeau and Belmont 2001). Magnetosheath turbulence is fundamentally based on mirror mode wave activity (Sahraoui et al. 2003). Dissipative mechanisms for collisionless shocks are also thought to be strongly related to wave activity (Krasnosselskikh et al. 2003). Therefore the THEMIS SCM instruments should not only gather crucial data for substorm studies but also for all the main fundamental processes controlling the physics of collisionless plasmas, namely shocks, magnetic reconnection, turbulence, plasma acceleration, transport and heating. In Sect. 2, we briefly present the science objectives also detailed in a companion paper (Roux et al. 2008). Section 3 is devoted to the presentation of the data reduction especially the calibration and spurious noise reduction process needed for the scientific use of SCM data. Preliminary science results are discussed in Sect. 4 for different regions, from the solar wind to the magnetotail, via magnetosheath and magnetopause.

# 2 Science Objectives

The primary goal of the Time History and Macroscale Interaction during Substorms (THEMIS) mission is to establish when and where substorms start, and to use this information to resolve the controversy about what instability triggers them (Angelopoulos et al.



2008). The main difference between the two types of models is the sequence of events that leads to the breakup (see for instance Lui 2001; Baumjohann et al. 2007). For the first type of model, magnetic reconnection (MR), presumably associated with the development of the tearing instability, is the trigger. In the second type of model, labeled as "Current Disruption" or CD, the breakup is triggered by a reduction in the cross-tail current associated with the development of an instability. In both cases ULF and ELF waves are expected to play a critical role.

In recent versions of the MR models (Mandt et al. 1994), whistler mode waves are expected to accelerate electrons up to very large (super-Alfvénic) velocities, thereby enhancing the reconnection rate. It has also been suggested (Bulanov et al. 1992; Attico et al. 2002) that very thin current sheets can be destabilized directly by HF tearing in the whistler mode range. On the other hand, in CD models the cross tail current can be directly disrupted by HF cross field instabilities, or undergo a low frequency (ballooning mode) instability coupled via div J=0 to parallel currents, which eventually drives ion cyclotron and/or whistler mode instabilities. The modeling of the latter instabilities is made difficult by the fact that electron bounce frequency in the magnetotail is around the proton gyrofrequency. Therefore the proper handling of HF frequency current driven instabilities should take into account the electron bounce motion and the corresponding electron bounce resonance (Karpman et al. 1977). Thus the identification of the waves, at substorm breakup (and during the expansion phase), is an important clue toward understanding what triggers substorms.

Together with the EFI instrument, which measures electric fields in the same frequency range, the Search Coil Magnetometer (SCM) will determine the nature of the waves that develop at breakup and during the expansion phase and, in the case of guided waves, remotely track the active region where breakup starts. The SCM is also needed to assess whether waves are electrostatic (such as lower hybrid waves) or electromagnetic (such as whistler mode waves). Thus wave observations provide a critical test to substorm scenarios and could provide a remote sensing of substorm dynamics during the expansion phase.

#### 3 Data Reduction

# 3.1 Reminder on THEMIS Coordinate Systems

Raw data are recorded in the sensor magnetic coordinate system for which the axes are defined by the magnetic axes of the search coils (see also Roux et al. 2008). Figure 1 displays the SCM antennas at the tip of the boom and gives the angles between the antenna axes and the probe geometric axes. In order to express data in a geophysical frame such as the GSE we need to perform the following coordinate transformations by the application of appropriate rotation matrices (see for more details Quinn et al. 2006):

- (1) Data are moved from the sensor magnetic coordinate system to the sensor mechanical coordinate system (SMC); actually these frames can be considered as identical.
- (2) Then data are moved from this latter frame to the spinning probe geometrical coordinate system (SPG) for which X axis corresponds to the ProbeX axis (see Fig. 1) and the Z axis is along the geometric Z axis (U2G matrix, see Table 1), the origin being at the geometric probe center.
- (3) Data are transformed from the SPG frame to the spinning sunsensor L-vectorZ (SSL) coordinate system, for which the *X* is directed toward the sun and the *Z* axis along the spin axis (G2S matrix, see Table 1).



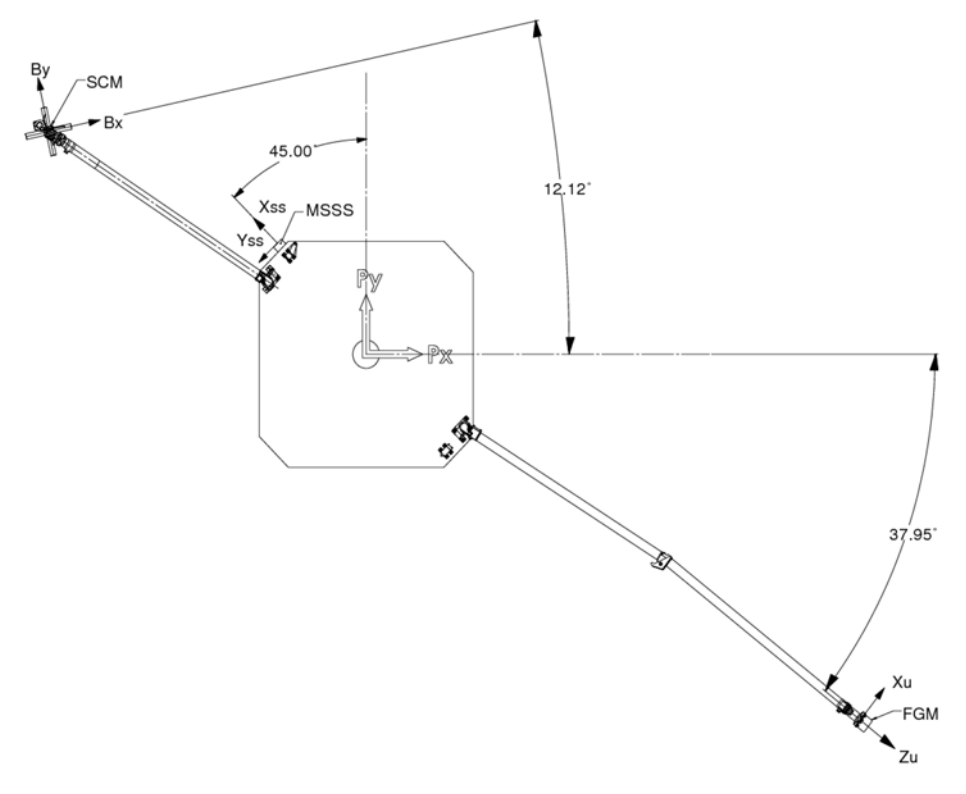


Fig. 1 Detail of sun sensor coordinates from SSL/UCB

Table 1 Matrices of rotations: Matrix U2G from Sensor mechanical coordinates (SMC) to probe geometric coordinates (SPG); Matrix G2S from Probe geometric coord. (SPG) to probe spin-Sun sensor coord. (SSL)

U2G			G2S		
0.9777	-0.2100	0.00000	-0.7071 $-0.7071$ $0.0031$	0.7071	0.0000
0.2100	0.9777	0.00000		-0.7071	0.0044
0.0000	0.0000	1.00000		0.0031	1.0000

(4) Finally, data are moved into a nonspinning system named Despun Sun L-vectorZ (DSL) obtained by a rotation about the spin axis by an angle equal to the opposite of the spin phase in the direction of the spin; the *X* axis is directed toward the sun and the *Z* axis corresponds to the spin axis.

# 3.2 SCM Calibration Method

The raw signal in Volts must be calibrated to physical units (nT). Each antenna response is characterized by its own transfer function, giving the ratio V/nT for a given frequency (for more details see Roux et al. 2008). These functions not being linear in frequency, a dedicated process must be applied to calibrate the raw waveforms. Basically two methods of calibration exist:

(1) Perform the Fourier Transformation (FT) of the signal, on a given time period, then divide by the complex transfer function to take into account amplitude correction and



phase shift; note that one has to fix a lower cut off frequency  $f_c$  as the transfer function goes to zero at null frequency. Finally perform an inverse FT to get the calibrated signal in the time domain.

(2) Deconvolve the instrument impulse response from the signal in the time domain.

The second method is implemented in the SCM calibration routine of the THEMIS software package; this method permits us to use optimized IDL convolution routines and gives better results in terms of computing time. The convolution is performed using a sliding window in order to provide a continuous calibration process.

Calibration of a SCM mounted onboard a spinning spacecraft with a spin frequency in the antenna bandwidth such as THEMIS probes requires additional steps compared with laboratory calibration. Indeed the components of the DC magnetic field perpendicular to the spin axis are measured as a sinusoid with a large amplitude at the spin frequency. Since this DC field ( $\simeq 100 \text{ nT}$ ) is about 100 times larger than the wave amplitude ( $\simeq 1 \text{ nT}$ ), it has to be removed from the raw signal before calibration to avoid undesirable effects. Furthermore the spinning motion at  $f_s$  introduces a Doppler shift: a circular wave at frequency  $f_L$  turning in the opposite direction of the satellite is measured by the sensor as a wave at frequency  $f_L + f_s$  whereas a wave turning in the same direction at  $f_R$  is measured as a wave at frequency  $f_R - f_s$ . Therefore sensors mounted onboard a spinning spacecraft are not able to fully restitute spin-plane fluctuations with frequency around the spin frequency. Indeed any circular waves turning in the same direction as the spin rotation are not detected because their apparent frequency becomes null. This also means that the sensitivity of the experiment at low frequency depends on the polarization of the waves with respect to the spin axis. Practically it is recommended before analyzing waves in a fixed frame (DSL, GSE, GSM, ...) to low-pass filter the data at a minimum frequency higher than the spin frequency; typically Fmin could be fixed to the sum of the spin frequency  $f_s$  and the cut off frequency  $f_c$ .

We distinguish a few different steps in the SCM calibration process (also described in the header of the THEMIS IDL calibration routine for scm data called thm\_cal\_scm available in the THEMIS software package). Different kinds of output may be useful to different users, and can be obtained using the following values of the step keyword in the IDL function:

# step 0: waveform in counts unit

Each data gap is time tagged and NaN symbols (Not a Number) are inserted for proper plotting. This step corresponds to raw data expressed in telemetry units.

**step 1:** waveform in Volts, spinning sensor system, with DC field

The conversion factor from telemetry units to volts is applied to the data but the spin modulation is still present.

**step 2:** waveform in Volts, spinning sensor system, without DC field

By using a sliding window of about two spin periods, we estimate the amplitude and phase of the spin signal on the three (x, y, z) components of the signal delivered by the sensors; the x-y amplitude and phase provides a measurement of the component perpendicular to the spin axis of DC magnetic field. This DC magnetic field can be expressed in the DSL system and can be compared to the FGM data, while the amplitude along Z allows the computation of the misalignment angle between the Z sensor axis and the spin axis. Note that the number of spin periods used for the sliding window can be fixed by the n\_spinfit keyword. At this step, these DC field components are removed from the signal. Furthermore, a special detrend method can be applied to perform a more efficient rejection of the spin signal and its harmonics, but frequencies below the detrend frequency are strongly reduced. This treatment can be applied using the Fdet keyword that allows specification of the detrend frequency. Finally during this step, a special noise reduction method can be also



applied to reject spacecraft-related spurious tones characterized during the commissioning. The spurious noise reduction process is described in the next subsection.

**step 3**: waveform in nT, spinning sensor system, without DC field

Calibrated waveforms for which the DC magnetic field variation has been removed. Note that data are still in a spinning frame associated with the sensors. The calibration is performed using a convolution kernel with a number of points fixed by the nk keyword. The choice of the value of nk involves a trade-off between quality of the low-frequency calibration and data processing speed. By default, an optimal value is chosen for each of the data modes, as a multiple of the sample frequency. For fast survey mode (scf mode with fe = 8 S/s nominally, where fe is the sampling frequency),  $nk = 8 \cdot fe$ . For particle burst mode (scp mode with fe = 128 S/s nominally),  $nk = 4 \cdot fe$  and for wave burst mode (scw mode with fe = 8192 S/s nominally), nk = fe. The mk keyword can be used to select a different multiple of the sampling frequency.

**step 4**: waveform in nT, spinning SSL system, without DC field
Same as step 3 but now data are in the SSL system using matrix of Table 1.

**step 5**: waveform in nT, fixed DSL system, without DC field, filtered

Data are now calibrated, without DC magnetic field variations, and are projected to a fixed frame common to all instruments (DSL). After this step, the SCM waveform can be transformed into any physical frame (GSE, GSM, etc.) using the cotrans routine available in the THEMIS software package. Note that after coordinate transformations the three original components will be mixed. Therefore it is important to ensure that before the change of frame the parallel and perpendicular components to the spin axis have undergone the same level of filtering. Thus at this step it is recommended to low-filter the three components with the same minimum frequency (fmin being fixed also as a keyword).

step 6: waveform in nT, fixed DSL system, with xy DC field

Same as step 5 but the calculated DC magnetic field components perpendicular to the spin axis are added to the waveform. *X-Y* components can be compared to the FGM data for cross-calibration. The *Z* component is unchanged.

#### 3.3 Spurious noise reduction process

First data analysis during commissioning showed that two types of noise with unexpectedly high amplitudes were present in the SCM waveform data. First, the power system produces a tone at twice the spin frequency (1/3 Hz) and its harmonics. As expected, the level of these tones decreases during eclipse period. Secondly, tones at 8 and 32 Hz, and their harmonics, were found to dominate the spectrum at higher frequencies. The frequencies of these tones correspond to the frequencies of instrument clocks onboard the spacecraft. At the present time it has not been possible to identify the exact source of the spurious noise. However we know that the 8 and 32 Hz are due to radiated noise, as their levels strongly decreased after SCM boom deployment (-10 dB).

Fortunately both type of spurious noises are locked in phase and relatively constant in amplitude. Spin tones are locked to the spin phase whereas the 8/32 Hz tones are phase locked with the onboard 1 s instrument clock. Thanks to this property it was suggested that a superposed epoch analysis (SEA) could reduce the level of these two types of phase locked noise (C. Chaston; private communication). Therefore a noise reduction process was developed based on two successive SEAs. A SEA consists of cutting the waveform data of duration T into N windows of definite duration ( $t_w \ll T$ ), named hereafter averaging windows. These N windows are superposed, or summed, which gives an average profile of the phase locked noise. Then a "noise waveform" of duration T is built by duplicating N



times the averaged noise. Finally the noise waveform at appropriate phase is subtracted from the raw waveform.

The spurious noise reduction process can be summarized as: (1) a first SEA with an averaging window equal to a multiple of the spin period, (2) a second SEA with an averaging window equal to a multiple of 1 s. The noise reduction process has been implemented in the current THEMIS software; two versions of the noise reduction routine are available and can be activated (or not) in the SCM calibration routine by fixing the keyword clnup\_author (clnup\_author = 'ole' by default or can be 'ccc'). Basically they give same results but algorithms are slightly different (see code sources for more details). Different levels of noise reduction can be selected for each version by using specific keywords (cleanup = 'spin' for only spin tone cleanup or 'full' for spin tones and 8/32 Hz cleanup). Note that the duration in seconds of the first and second averaging windows can be fixed by the keywords wind dur spin and wind dur 1s respectively.

Figure 2 displays the different stages of the noise reduction process on particle burst data (128 S/s). Note that some spikes remain after this process. They come from noise which is not phase locked therefore not eliminated by SEA.

Figure 3 displays spectra performed from SCM wave burst data (scw mode with 8192 S/s) on March 23rd 2007 between 135945 and 140216 UT. Data are despun and projected into the sensor coordinates system in order to be compared with data measured at the laboratory. As in the example of figure 2, 8/32 Hz tones are strongly reduced by noise reduction process but still present in the spectra as other spikes which are not phase locked. However, we see that these in flight measurements give the same Noise Equivalent Magnetic Inductions (NEMI) as reported in (Roux et al. 2008):  $0.4 \text{ pT}/\sqrt{\text{Hz}}$  at 10 Hz,  $0.08 \text{ pT}/\sqrt{\text{Hz}}$  at 100 Hz for Bz and 0.15 for Bx and By and  $0.01 \text{ pT}/\sqrt{\text{Hz}}$  at 1 kHz. In-flight NEMIs can be smaller than NEMIs in the laboratory if the in-flight temperatures of the preamplifiers and sensors are lower than at laboratory (273 K). Note that the higher level of noise on Bx and By between 15 Hz and 1 kHz is found only on Bx in the SSL frame, and is therefore related to the sun sensor direction (Ludlam et al. 2008).

#### 4 Science Results

In this section we present first examples of THEMIS data from the solar wind to the magnetotail.

4.1 Solar wind-magnetosheath-dayside magnetosphere regions: June 21st 2007 event

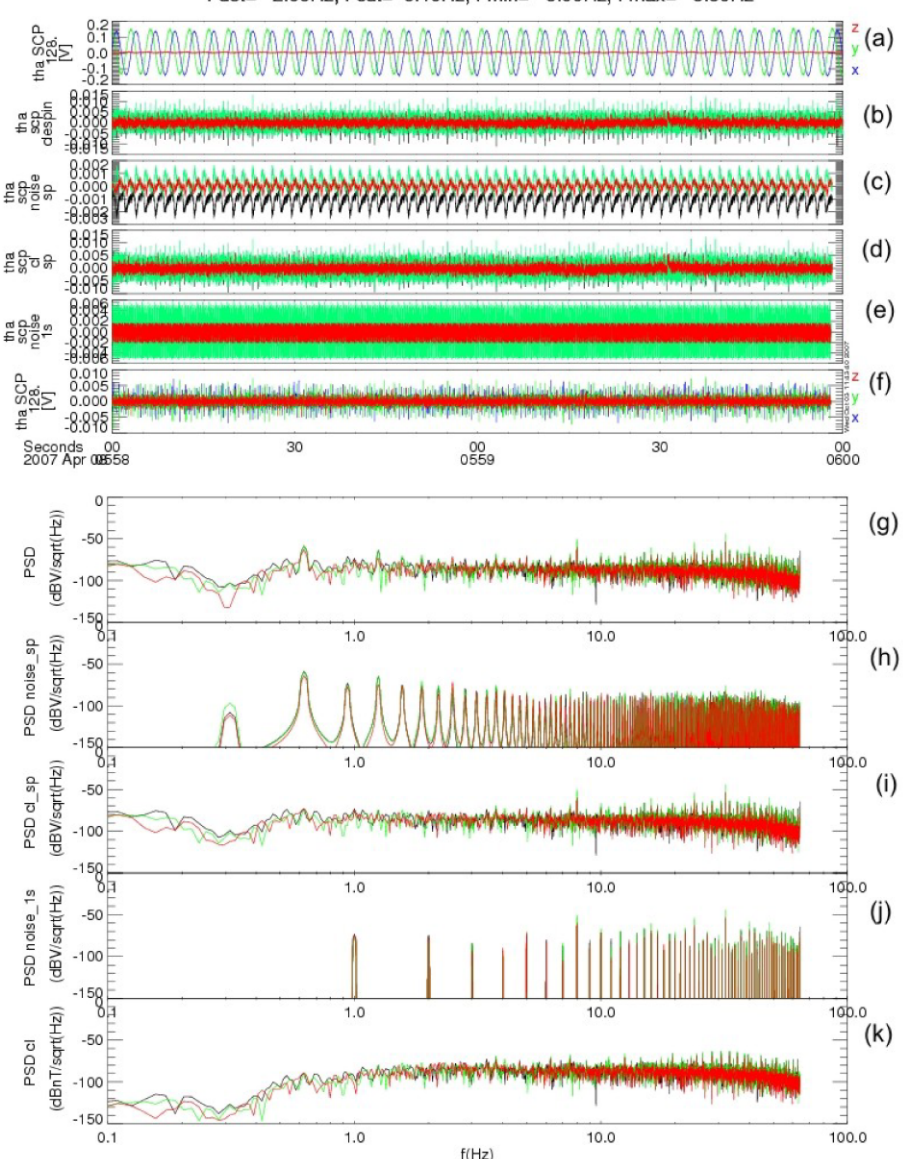
Figure 4 shows the position in the GSE frame of the THEMIS constellation on June 21st from 0800 to 1050 UT. Around 0800 UT, THEMIS-A (THA) is the farthest probe from the earth whereas THB is the closest one; probes c, d and e are slightly separated along Y but almost at the same X in between a and b. The selected time period displayed in Fig. 5 corresponds to a fast survey mode. In this mode, FGM data (Auster et al. 2008) have 0.25 s time resolution (panels a, b, c and d). Ion ESA data (McFadden et al. 2008) including moments ( $n_i$ ,  $V_i$ ,  $T_i$ ) have 3 s time resolution (panels e, f, g, and h), and electron fluxes are available with the same time resolution (panel i). SCM waveform data have 0.125 s time resolution (scf mode) from which we construct spectra at 32 s resolution (panels j, k, l, and m).

For most of the selected time period THA is located in the solar wind as illustrated by Fig. 5. Indeed from 0800 to 1015 UT, the magnetic field modulus is smaller than 10 nT (panel d), the average ion energy is around 800 eV (panel e) with  $n_i \simeq 10 \,\mathrm{p\cdot cm^{-3}}$  (panel f),  $V_x \simeq -350 \,\mathrm{km\cdot s^{-1}}$  (panel g) and  $T_i \leq 50 \,\mathrm{eV}$  (panel h).



#### SCM calibration parameters:

Nk= 8192, Step=2 ,Despin=1, N\_spinfit=2, cleanup (ole)=full, 1st av. wind.=3.20, 2nd av. wind.= 1.0,
Fdet= 2.00Hz, Fcut= 0.10Hz, Fmin= 0.00Hz, Fmax= 0.00Hz



SCM FFT parameters: Nbps = 8192, Sample Period (s) =0.00781250, df (Hz) =0.015625, FFT duration (s) =64.000, wind =1

Fig. 2 Search coil particle burst data recorded by THEMIS-A (THA) on April 8th, 2007 between 0558 and 0600 UT. From top to bottom: (a) scm raw waveform in volts, (b) despinned waveform, (c) spin phase locked noise built by applying SEA, (d) cleaned (only power ripples) waveform, (e) 1 s phase locked noise waveform (SEA), (f) fully cleaned waveform, corresponding spectra in dBV/ $\sqrt{\text{Hz}}$  follow in the same order except for despinned waveform data: (g) spectrum of (b), (h) spectrum of (c), (i) spectrum of (d), (j) spectrum of (e), and (k) spectrum of (f). Tones at  $2f_s$ ,  $4f_s$ , 8 and 32 Hz are strongly reduced. However, note that at the end of noise reduction process (panel k) some spikes are still visible at high frequencies due to the fact that they come from noise which is not phase locked



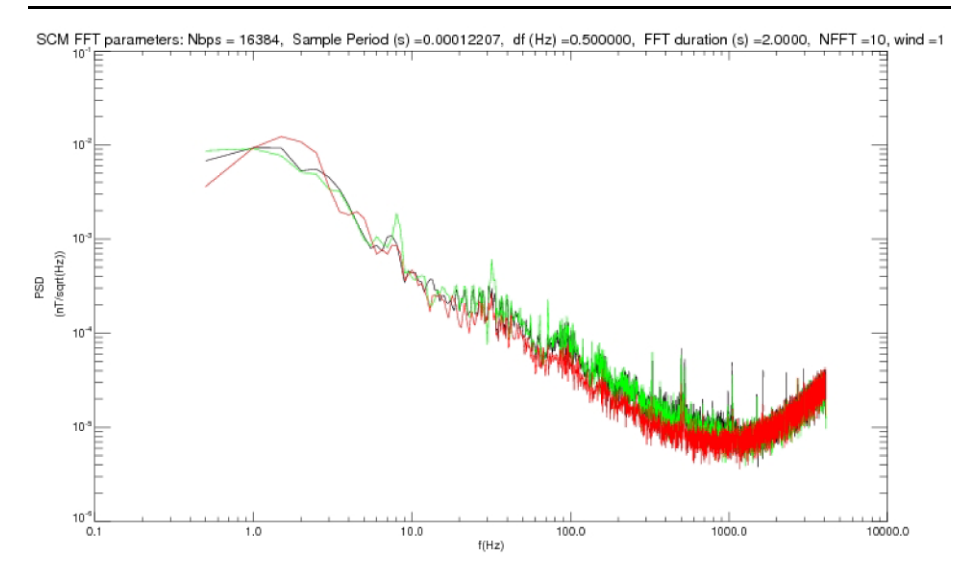


Fig. 3 Spectra of SCM data during a wave burst period (scw mode) on March 23rd 2007 from 1359:45 to 1400:16 UT. Data are in sensor coordinate system (step 3), with nk = 16384, Despin = 1, Fdet = 2, and a full noise reduction with wind\_dur\_1s = 1

Average electron energy (panel i) is no more than 15 eV which is consistent with the characteristics of the slow solar wind around 1 astronomical unit. At 1015 UT THA crosses the shock and the modulus of B increases from 5 to 15 nT, the  $V_x$  component of the ion velocity decreases from 400 to 150 km·s<sup>-1</sup>, the ion density increases from 10 to more than 40 p·cm<sup>-3</sup> and the ion temperature increases from less than 70 eV to more than 200 eV. Therefore the solar wind slows down and is heated as it goes through the collisionless shock. The amplitude of magnetic fluctuations in the ultra low frequency (ULF) range is maximum at the shock crossing ( $\simeq$ few nT) with frequencies up to (at least) 4 Hz, while it is less intense ( $\le$  1 nT) and mainly below 1 Hz in the magnetosheath after 1014 UT.

In addition to the shock crossing described above, wave and ESA data give evidence for smaller perturbations (0825, 0850, 0925 and 1000 UT) which look like very brief shock crossings or approaches. Notably the sharp signature around 0850 UT has the same characteristic as the shock crossing (velocity decrease, temperature and density increases, strong wave activity up to 4 Hz). It could correspond to a fast sunward and then earthward motion of the shock. Unlike the 1050 UT shock crossing, however, energetic ions are also detected together with the magnetic perturbations, which tells us that the probe penetrates into the foreshock before possibly crossing the shock.

In Fig. 6, the same set of data is displayed, but now gathered by THB (the closest to the earth). THB is almost always into the magnetosheath during the selected time period except between 0920 and 0930 UT when it briefly crosses the shock, and after 1020 UT when it enters into the magnetosphere. During the period where probe b is in the magnetosheath, the amplitude of ULF magnetic fluctuations varies strongly (panels j, k, l and m); probe b records three intensifications (0825, 0850, and 1000 UT) up to 15 nT, well above the average magnetosheath amplitude ( $\leq 1$ –2 nT) in addition to the intensification associated with the shock crossing at 0925 UT. These intensifications seem to correspond in a one-to-one fashion with the small perturbations observed on THA data in the solar wind (discussed



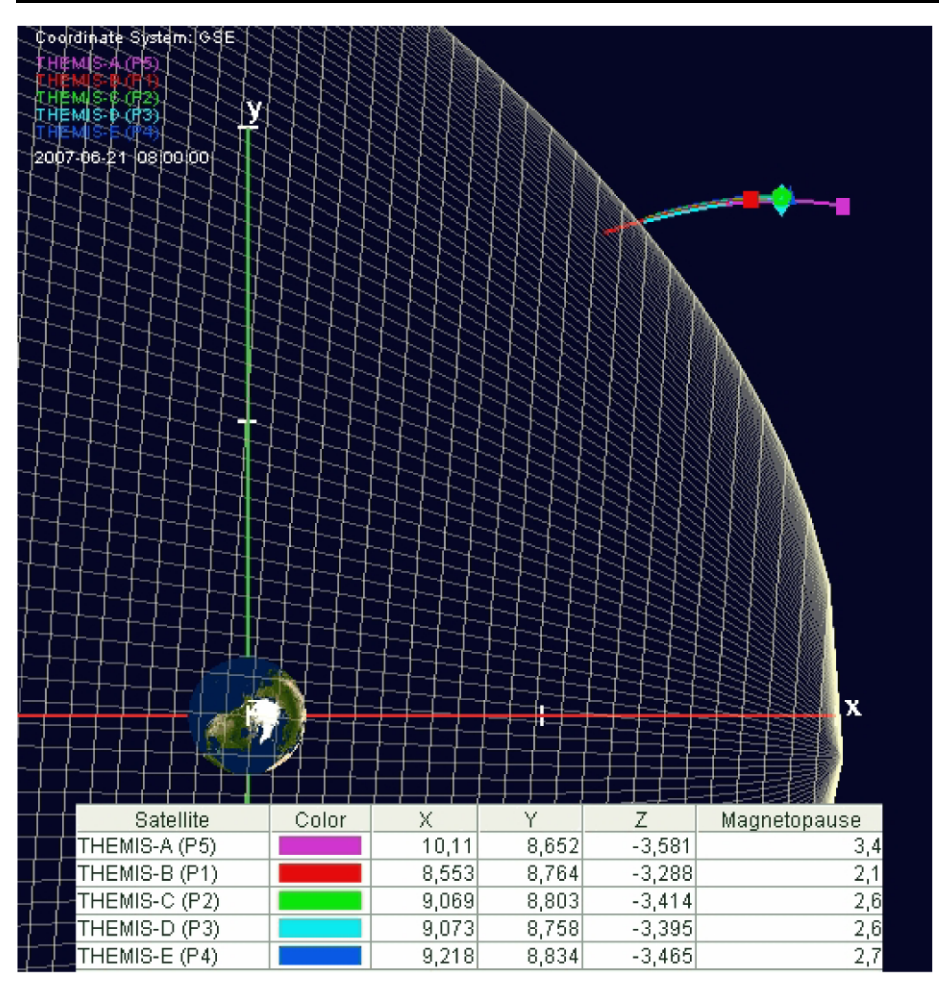
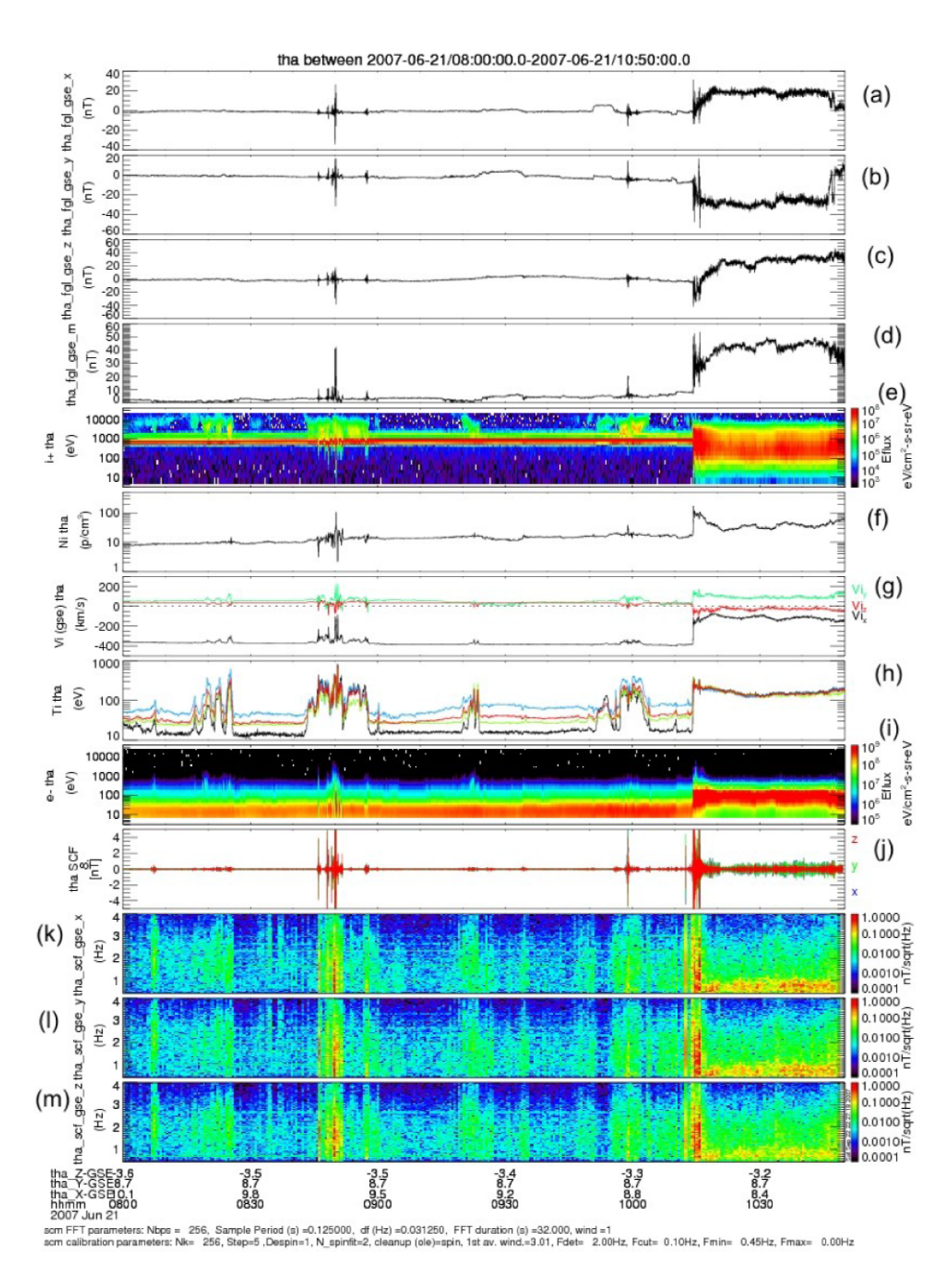


Fig. 4 THEMIS probe locations (GSE,  $R_E$ ) on June 21st 2007 between 0800 and 1050 UT (This product is available at http://sscweb.gsfc.nasa.gov/tipsod). Satellite locations are also tabulated in GSE coordinates at 0800 UT. Magnetopause location for a solar wind dynamic pressure of 3.5 nPA (obtained from WIND survey) is also shown as well as distance to the magnetopause for each probe

above). Yet the amplitudes of the magnetic fluctuations are larger by a factor of 5–10 in the magnetosheath, and an amplification mechanism has to be invoked.

Also, the magnetopause crossing detected by THB (1018 UT) turns out to occur four minutes later than the shock crossing detected by probe a (1014 UT), which suggests a sunward global motion of both the magnetopause and the shock. In addition to this global outward motion, quasi-periodic perturbations convected by the solar wind lead to ion foreshock crossings and even skimming along the bow shock. Cluster and Geotail are located close to the magnetopause in the dawnside and dusk sector, respectively. They also detect magnetopause crossings during the same time period. Thus this event is particularly well suited to conduct a global analysis of the shock/magnetopause response to solar wind perturbations.





**Fig. 5** From *top* to *bottom*: panels **a**, **b**, **c**, and **d** correspond to Bx, By, Bz and B (FGM data), ion energy spectrogram (panel **e**), density (**f**), velocity (**g**) and temperature (**h**), panel **i** corresponds to electron energy spectrogram (ESA data), panels **j**, **k**, **l**, and **m** display waveforms and spectrograms of Bx, By and Bz fluctuations from 0.45 to 4 Hz, (SCM data)



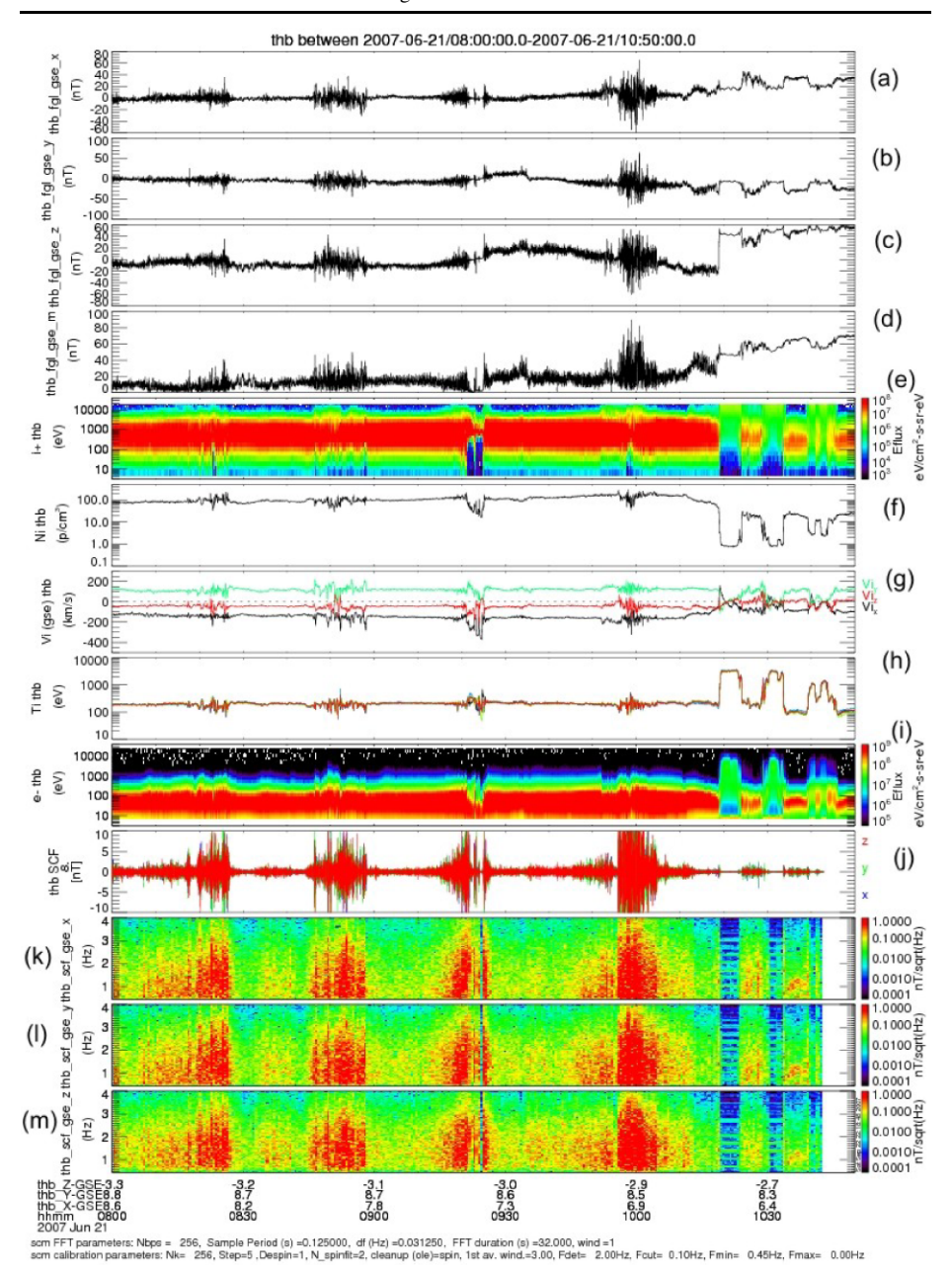


Fig. 6 Same legends as Fig. 5

# 4.2 Flux Transfer Event: May 20th 2007

On May 20th, 2007, the 5 THEMIS spacecraft encountered a Flux Transfer Event (FTE). Figure 7 shows the locations of the five spacecraft in GSE. Notice that Y is of the order of 12.5  $R_E$ , while X is of the order of 5.5  $R_E$ , so that the satellites were located in the afternoon



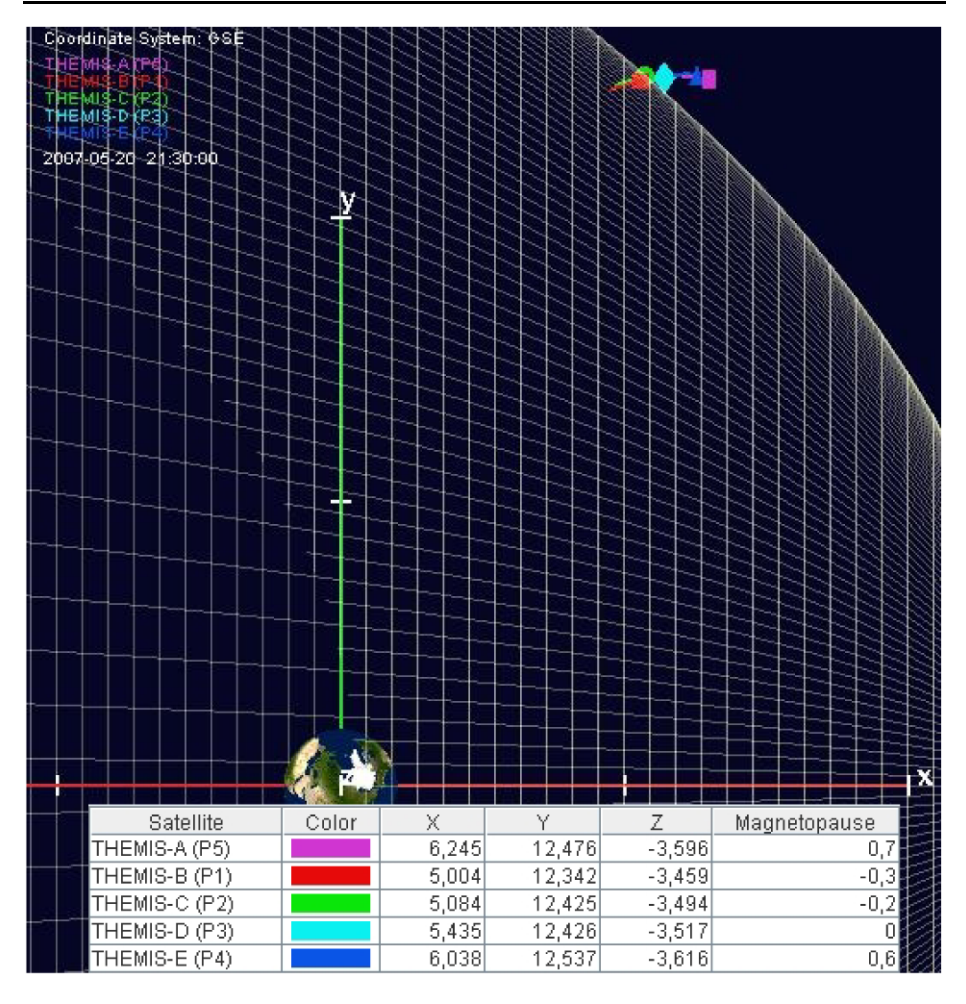


Fig. 7 THEMIS probe locations (GSE,  $R_E$ ) on May 20th 2007 between 2130 and 2230 UT. Satellite locations are also tabulated in GSE coordinates at 2200 UT. Magnetopause location for a solar wind dynamic pressure of 1 nPA (obtained from WIND survey) is also shown as well as distance to the magnetopause for each probe

sector. This spacecraft configuration is particularly interesting since the five satellites bracket the FTE structure, with THB and THC on the magnetospheric side and THA and THE on the magnetosheath side, while THD is close to the magnetopause current layer as illustrated by the estimated distances to the magnetopause of each probe on Fig. 7.

The geometry of the FTE, and the general characteristics of this event will be discussed elsewhere (Sibeck and Angelopoulos 2008a; Sibeck et al. 2008b). Here we give a preliminary description of ULF wave observations inside and near the FTE, and suggest possible wave-particle interactions. For practical reasons we only show data from THC in Fig. 8; data from the other spacecraft are available and are discussed below. The magnetic structure of the FTE is clearer on THB, THC, and THD, located inside the magnetosphere and at the current layer, than on THA and THE, on the magnetosheath side. Panels a, b, and c of Fig. 8, show the 3 magnetic components in GSE, while panel d shows the modulus of *B*. THC, on



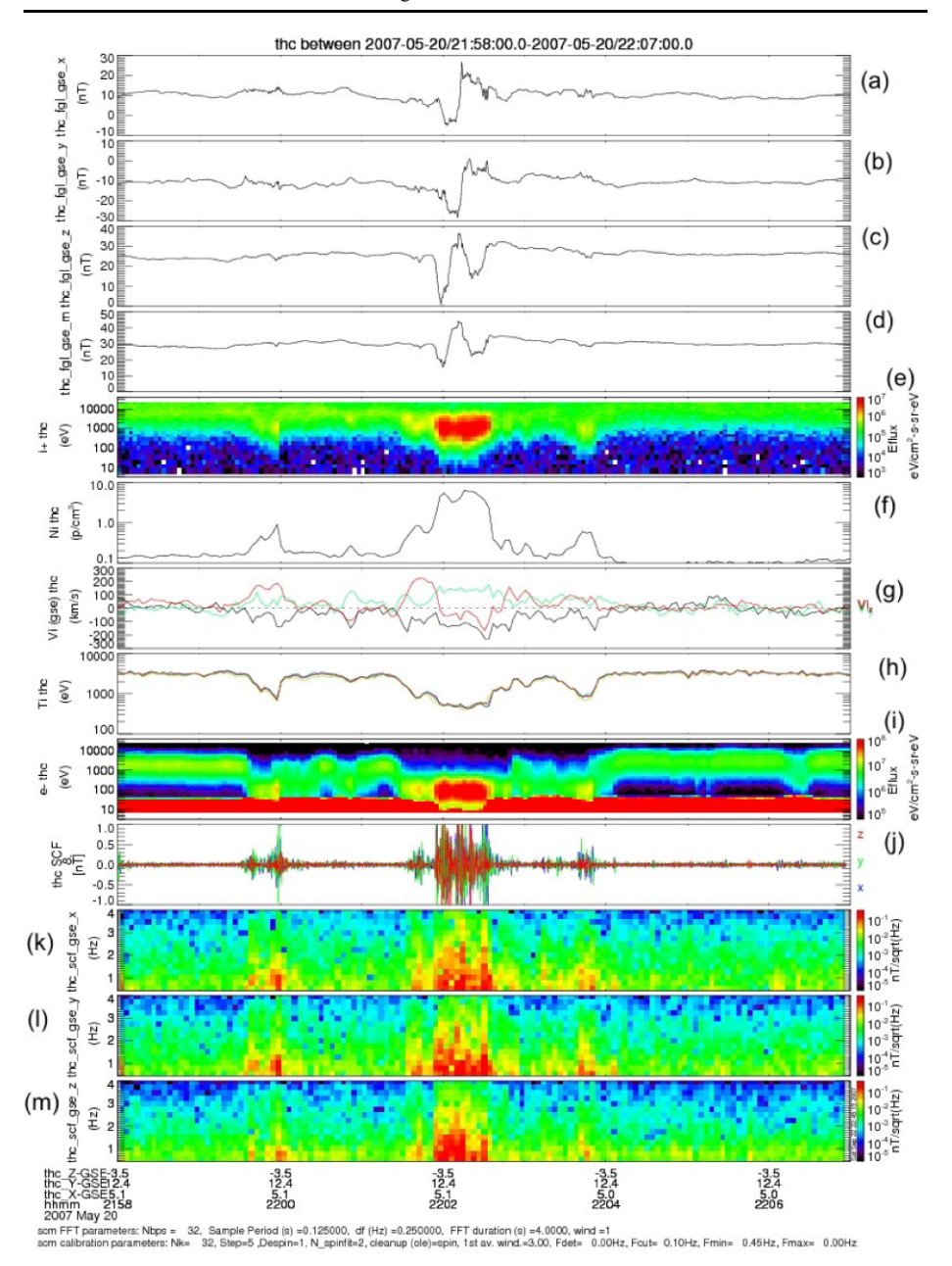


Fig. 8 Same legends as Fig. 5 but time resolution of spectra is 4 s

the magnetospheric side, observes a bipolar magnetic field signature of By, which is close to normal to the nominal magnetopause. A crater-like variation in the magnetic field strength is observed on THB (closest to the earth), and to a lesser extent on THC (see Fig. 8, panel d). On THD, at the current layer, a maximum in the modulus of B is found.



THC was first in the magnetosphere (before 2201:50), as evidenced by the large energies of electrons (panel i) and ions (panel e), and it returns to the magnetosphere after the FTE crossing (after 2202:30). As it penetrates the core of the FTE, THC observes increased ion flux, corresponding to: (i) heated magnetosheath plasma (panel e), (ii) enhanced densities, comparable to magnetosheath values (panel f), (iii) enhanced ion flow velocities (panel g), (iv) enhanced fluxes of accelerated or heated magnetosheath electrons (panel i) and (v) enhanced magnetic components of ULF waves (panels j to m). The simultaneity between the ULF waves and the particle acceleration/heating suggests that a wave-particle interaction process is at work. Can we use data from the other spacecraft to discriminate between possible wave interaction processes; in particular can we identify the particle species, electrons or ions, involved in the interaction with waves?

In the magnetosheath, THE and THA observe quasi-steady fluxes of magnetosheath ions. The flux and the energy bandwidth do not change as these spacecraft pass by the FTE, and ions are not correlated with variations in wave amplitude. On the other hand magnetosheath electrons (THE and THA), and current sheet electrons (THD) are also heated/accelerated in a region that is broader than the FTE, but this region coincides with wave observations.

In summary, ULF waves are observed together with accelerated/heated electrons. On the magnetospheric side these signatures coincide with that of the FTE, while on the magnetosheath side and at the current layer, ULF waves and heated/accelerated electrons are observed in a broader region (boundary layer). These preliminary observations suggest that electromagnetic waves interact with electrons inside the FTE on the magnetospheric side, and in a broader region comprising the current layer on the magnetosheath side. We will analyse wave characteristics, as well as the shape of the electron distribution function, and investigate possible signatures of wave particle interactions as a potential electron heating mechanism. More detailed studies based on the analysis of electron distributions are planned to confirm these preliminary results.

## 4.3 Magnetopause Crossing Event: June 19th 2007

Figure 9 displays the THEMIS constellation between 0800 and 1030 UT. THB is the leading probe, while THA is the trailing one; THC, THD, and THE follow almost the same trajectory. As the THEMIS constellation goes away from the earth it moves toward the duskside and out of the GSE equator.

The THEMIS instruments are in the fast survey mode during this time period (0800–1030 UT). THA is most of the time in the quiet magnetosphere, while the other probes leave the magnetosphere to enter the magnetosheath in the following order: THB, then THD and THC almost at the same time, and finally THE. Before staying definitely in the magnetosheath each probe undergoes multiple magnetopause crossings, hence the timing has to be considered in the averaged sense. Note that THD and THC undergo exactly the same number of magnetopause crossings although magnetic field or density profiles can be slightly different thereby indicating a temporal variation of the boundary during its motion.

Now we focus on the particle burst period recorded onboard THC between 0940:30 and 0944:00 UT shown on Fig. 10. In this mode FGM data are sampled at 128 S/s (panels a, b, c, and d), ion and electron moments from ESA data are available at 3 s resolution (panels e to l) and SCM data are sampled at the same rate as FGM (panels m to p).

All instrument signatures indicate that THC crosses the magnetopause and enters into the magnetosheath: the modulus of B decreases (from 45 nT to 30–35 nT), the particle den-



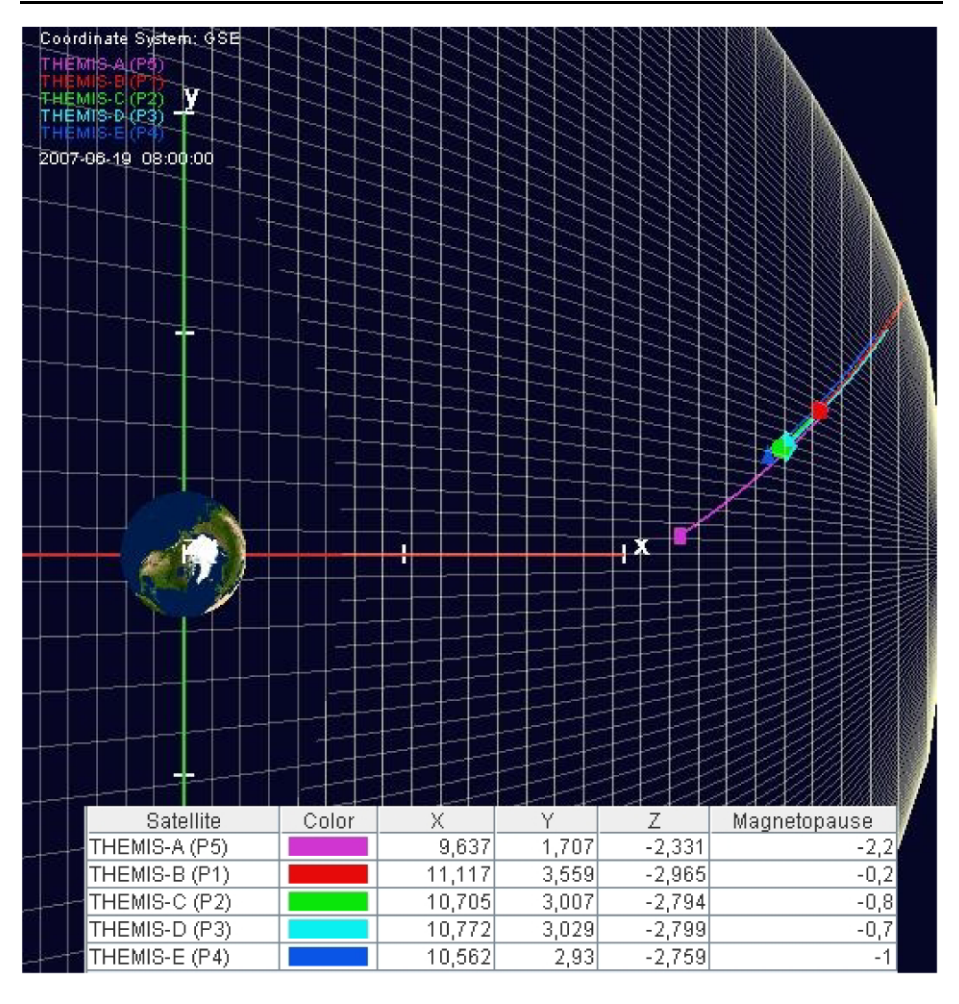
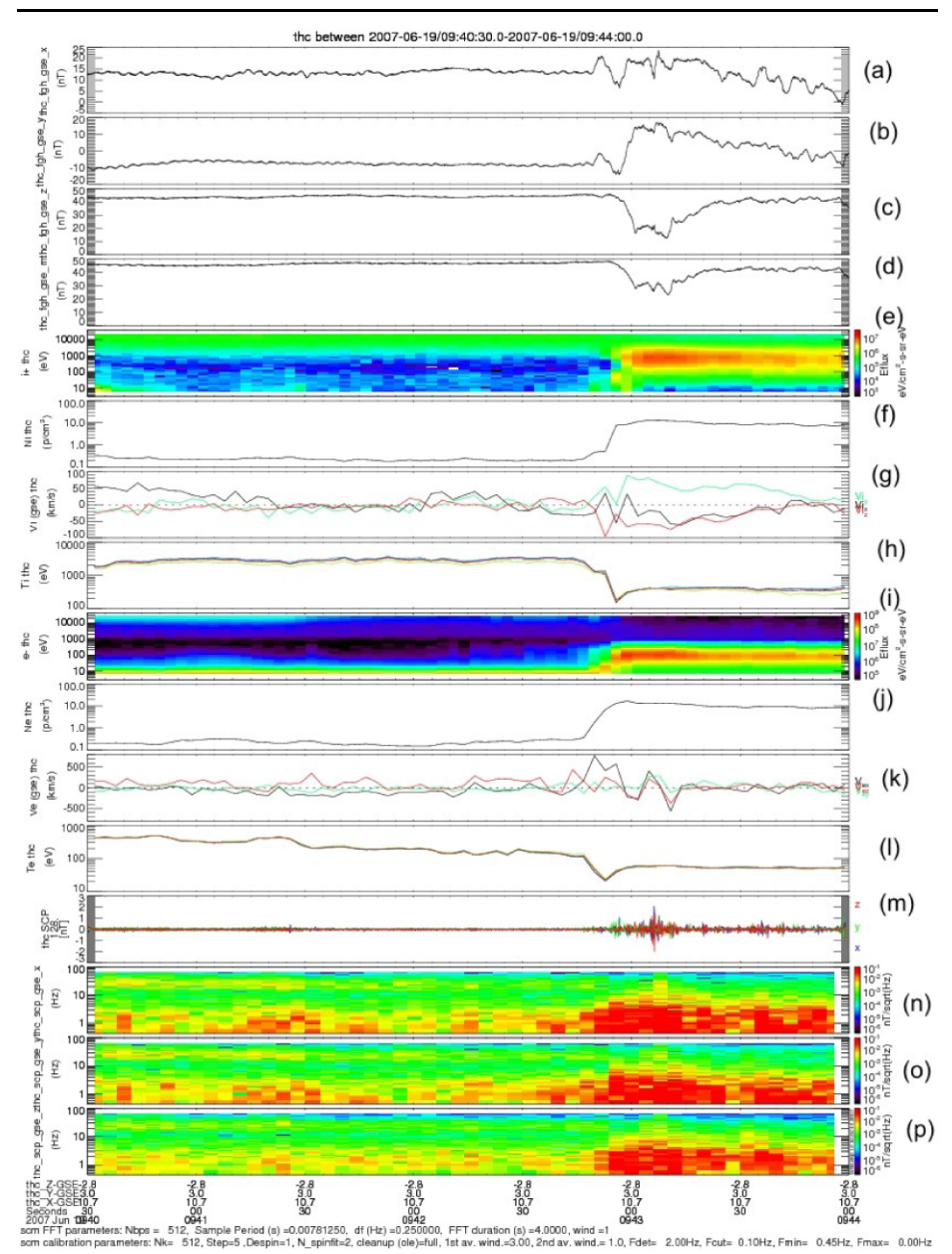


Fig. 9 THEMIS probe locations (GSE,  $R_E$ ) on June 19th 2007 between 0800 and 1030 UT. Satellite locations are also tabulated in GSE coordinates at 0943 UT. Magnetopause location for a solar wind dynamic pressure of 1 nPA (obtained from WIND survey) is also shown as well as distance to the magnetopause for each probe

sity increases (from 0.2 to 10 p·cm<sup>-3</sup>), while particle temperatures decrease (from 2 keV to 300 eV). The amplitude of the ULF magnetic fluctuations is maximum at the boundary; their frequencies increase up to 10 Hz as the probe crosses the magnetopause. Ion and electron fluxes as well as velocities are largest within the boundary and during the intense ULF magnetic wave activity. More investigations are needed to determine whether plasma transport occurs through the boundary and whether magnetic fluctuations play a crucial role in this transport. In particular, electron moments have to be carefully checked in such conditions where the density varies rapidly (see McFadden et al. 2008 for discussion on this instrumental issue). However we can already mention that an amplification of the magnetosheath turbulence at the magnetopause is expected by models and has been already observed by pre-





**Fig. 10** From *top* to *bottom*: panels  $\mathbf{a}$ ,  $\mathbf{b}$ ,  $\mathbf{c}$ , and  $\mathbf{d}$  correspond to Bx, By, Bz and B (FGM data), ion energy spectrogram (panel  $\mathbf{e}$ ), density ( $\mathbf{f}$ ), velocity ( $\mathbf{g}$ ) and temperature ( $\mathbf{h}$ ), electron energy spectrogram ( $\mathbf{i}$ ), density ( $\mathbf{j}$ ), velocity ( $\mathbf{k}$ ) and temperature ( $\mathbf{l}$ ) (ESA data), panels  $\mathbf{m}$ ,  $\mathbf{n}$ ,  $\mathbf{o}$ , and  $\mathbf{p}$  display waveforms and spectrograms of Bx, By and Bz fluctuations from 0.45 to 64 Hz (SCM data)

vious magnetospheric missions. Models show that it can lead to a plasma transport across the boundary (see for instance Rezeau and Belmont 2001).



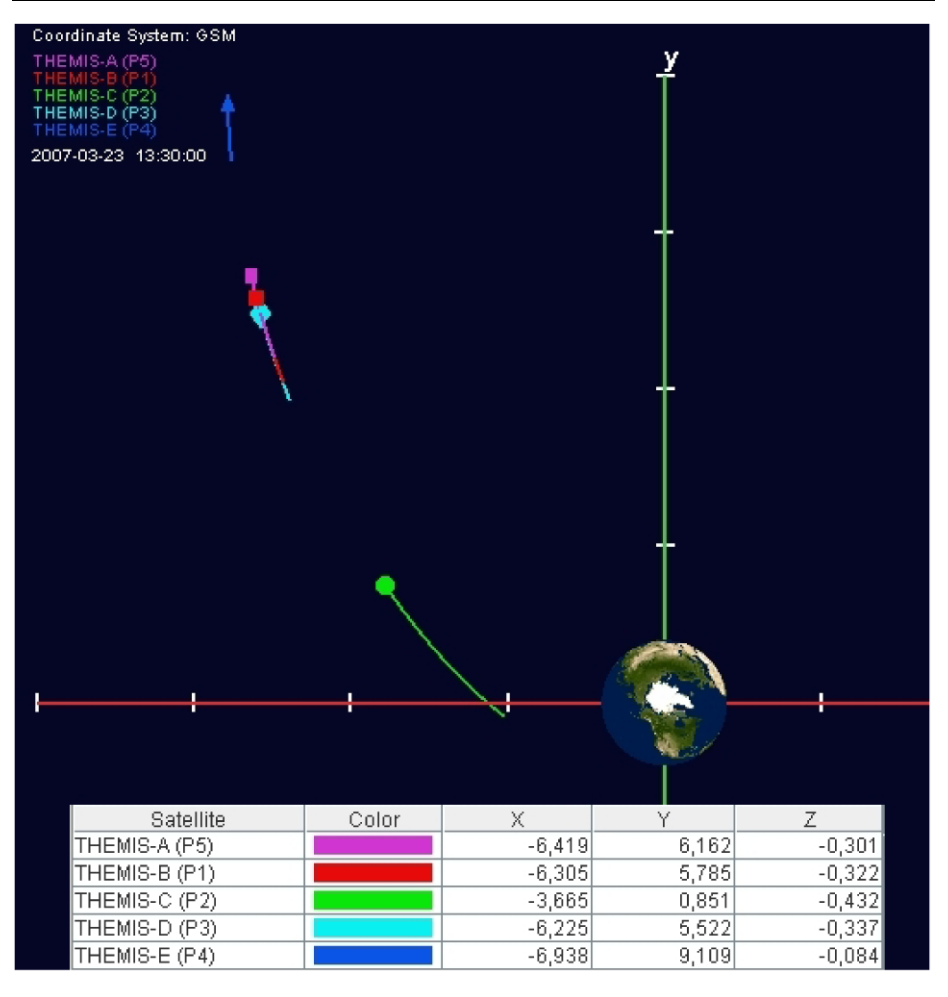


Fig. 11 THEMIS probe locations (GSM,  $R_E$ ) on Mars 23rd 2007 between 1330 and 1430 UT. Satellite locations are also tabulated in GSM coordinates at 1400 UT

### 4.4 Substorm Event: March 23rd 2007

Two substorms were captured on March 23rd 2007. THEMIS positions are plotted in Fig. 11 in GSM coordinates between 1330 and 1430 UT around the second local dipolarization. THC is the leading probe moving from the duskside toward the earth with THE trailing; THD, THB and THA are in between and following THC in this order. During this period the THEMIS constellation is located in the south hemisphere.

The first local dipolarization is observed by THC at 1114:30 UT while ground based observations and Polar data indicate an auroral substorm onset at 1113 UT dawnward of the mapped point of THC. This first dipolarization is analyzed in detail in (Angelopoulos et al. 2008). The order of the probe positions is the same as for the second dipolarization displayed in Fig. 11 and discussed later; the THEMIS constellation was also located in the dusk side but farther from the earth than during the second event, slightly closer to the equator. Here



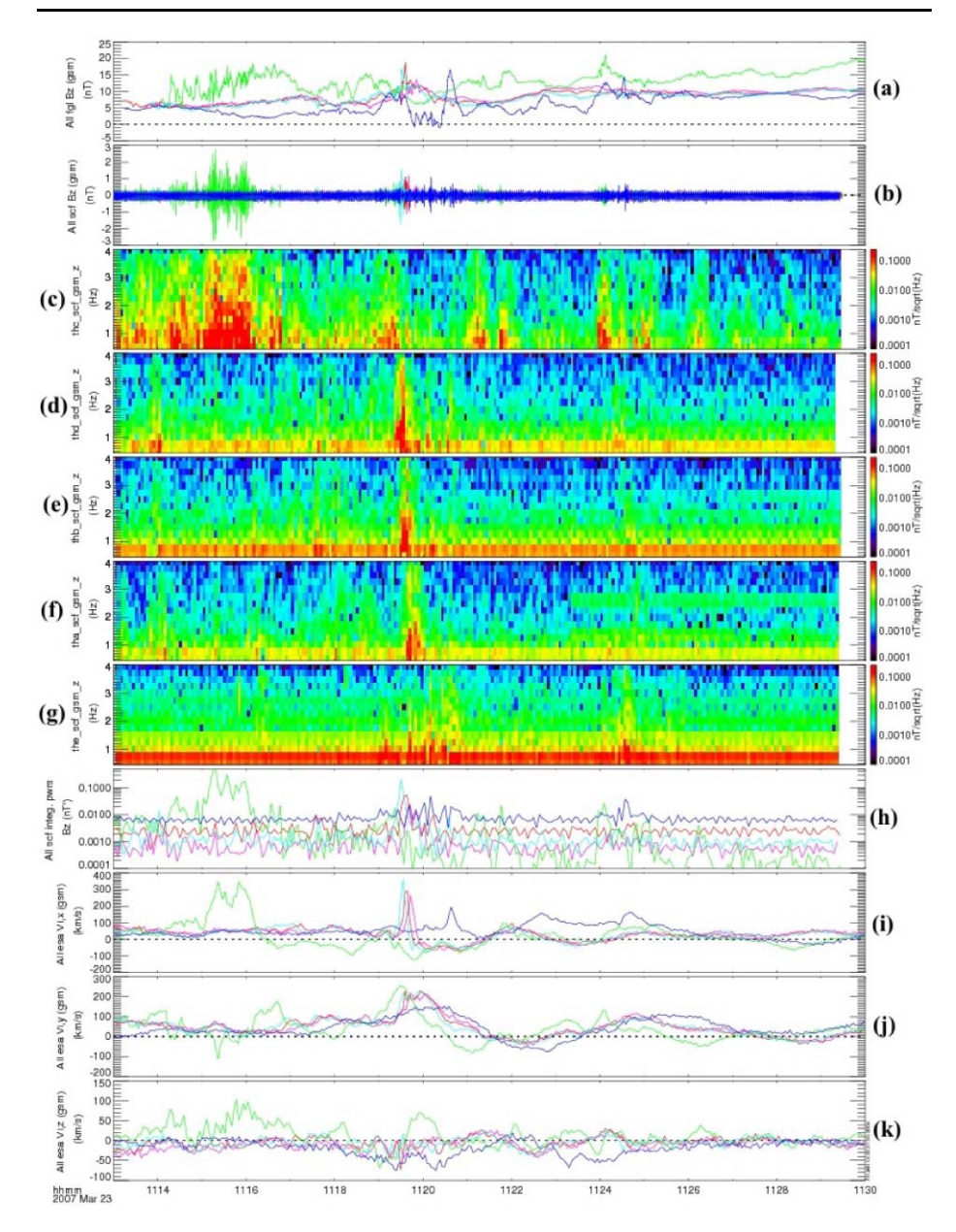


**Fig. 12** Five THEMIS probes data in fast survey mode on March 23rd 2007 between 1113 and 1130 UT. From *top* to *bottom* Panel **a**: Bz from FGM data with 0.5 s time resolution, panel **b**: Bz from SCM waveform data between 0.45 to 4 Hz, panels **c** (THC), **d** (THD), **e** (THB), **f** (THA), **g** (THE): SCM Bz power spectral densities, panel **h**: integrated powers from 0.45 to 4 Hz with 4 s time resolution for the 5 probes, panels **i**, **j**, **k**: x, y, and z components of the ion velocity with 3 s time resolution

we just show a summary plot around the first local dipolarization onset (Fig. 12) to compare with the second event discussed later in more details.



In panel a, the Bz component of the magnetic field is shown in GSM (FGM data) for the five probes. THC (green) clearly detects the dipolarization first while THD (cyan), THB (red), THA (magenta) and THE (blue) detect it later. The delays ( $\simeq$  67 s) between THD and THE ( $\Delta Y_{d-e} \simeq 2.5~R_E$ ) calculated from both Bz, from Vx or from Vy signatures (panel j) give an estimated azimuthal propagation velocity of about 240 km/s. This also agrees with the velocity inferred from ground-based and polar observations (for more details see Angelopoulos et al. 2008).

ULF Magnetic fluctuations amplitudes (panel b) as well as integrated powers (panel h) recorded by SCM in the range 0.45 to 4 Hz (scf data) increase at the dipolarization and are well correlated with the amplitude of the x component of the ion velocity (panel i). Most of the ULF magnetic activity is below 4 Hz (panels c, d, e, f, g) and around the proton cyclotron frequency ( $f_{c,i} \simeq 0.6$  Hz). Note that a high level of spurious noise below 1.5 Hz is still present despite of the noise reduction process; it is due to particular conditions during the commissioning on March 23rd. The ion velocity increases suddenly at the dipolarization especially on the Vx component up to 350 km/s on THC and THD (panel i).

Now we deal with the second dipolarization which starts first at 1358:30 UT on THD. This dipolarization is fortunately caught during a particle burst period. Unfortunately the POLAR cameras were not in a position to detect the substorm. Figure 13 displays an overview of THA data on March 23rd between 1330 and 1430 UT during a fast survey period. Panels a, b, and c show that the magnetotail stretches from 1330 to 1358:30 UT, as expected for a growth phase; the Bx and By components are increasing in modulus (from 25 nT to 33 nT, and from 35 nT to 55 nT, respectively). The THEMIS constellation is located in the dusk sector, so both Bx and By correspond to the main field components of the magnetotail. The dipolarization occurs suddenly at 1359 UT as Bz increases from 3 nT to 10 nT and By decreases from 55 nT to 45 nT. Magnetic low-frequency fluctuations are recorded (5–15 mHz) until the end of the dipolarization around 1410 UT when the Bz component reaches 16 nT while By  $\simeq$  35 nT. Panel e (SST data) and panels f, h, and i (ESA data) indicate that the ions are mostly accelerated and heated at the dipolarization onset while electrons seem to be accelerated in successive steps (panels j and k). Panel g shows a short lasting peak in the ion density profile at the beginning of the dipolarization onset and panel h gives evidence for low-frequency fluctuations on the three components of the velocity. Note that the oscillation on the Vy component of the ion velocity starts before the dipolarization. Finally panels l, m, n, and o show four intensifications of magnetic fluctuations during the dipolarization. Again most of the ULF magnetic fluctuations are below 4 Hz and around  $f_{c,i} \simeq 0.64$  Hz. Figure 14 is a detail of the dipolarization period data gathered by THA (magenta), THB (red), THD (cyan) and THE (blue). THC is too close to the earth and misses the dipolarization. Panel a shows that the increase of the Bz component starts first on THD ( $\simeq$ 1358:30 UT), then THB ( $\simeq$ 1358:50 UT), THA ( $\simeq$ 1359:00 UT) and finally on THE ( $\simeq$ 1400:20 UT). The delay ( $\simeq$  110 s) between THD and THE ( $\Delta Y_{d-e} \simeq 3.6~R_E$ ) calculated from both Bz signatures gives an estimated azimuthal propagation velocity of about 210 km/s; the same estimation using THA and THE gives 240 km/s. Panel b shows SCM Bz waveforms which give the same timing for the dipolarization onset. Note that the largest Bz amplitudes (SCM data) correspond to successive local dipolarizations (FGM data).

Panels c, d, e and f indicate for each probe (in the observed order of the dipolarization THD, THB, THA and THE) that the power spectral density increases suddenly at the dipolarization and is again maximum for fluctuations with frequencies below 4 Hz. Integrated power of the magnetic fluctuations between 0.45 and 4 Hz is plotted on panel g. These integrated powers are smaller ( $\simeq 5 \times 10^{-3}$ –3  $\times 10^{-2}$  nT<sup>2</sup>) than those recorded closer to the magnetic equator at the geostationary orbit (see for instance Perraut et al. 2000a;



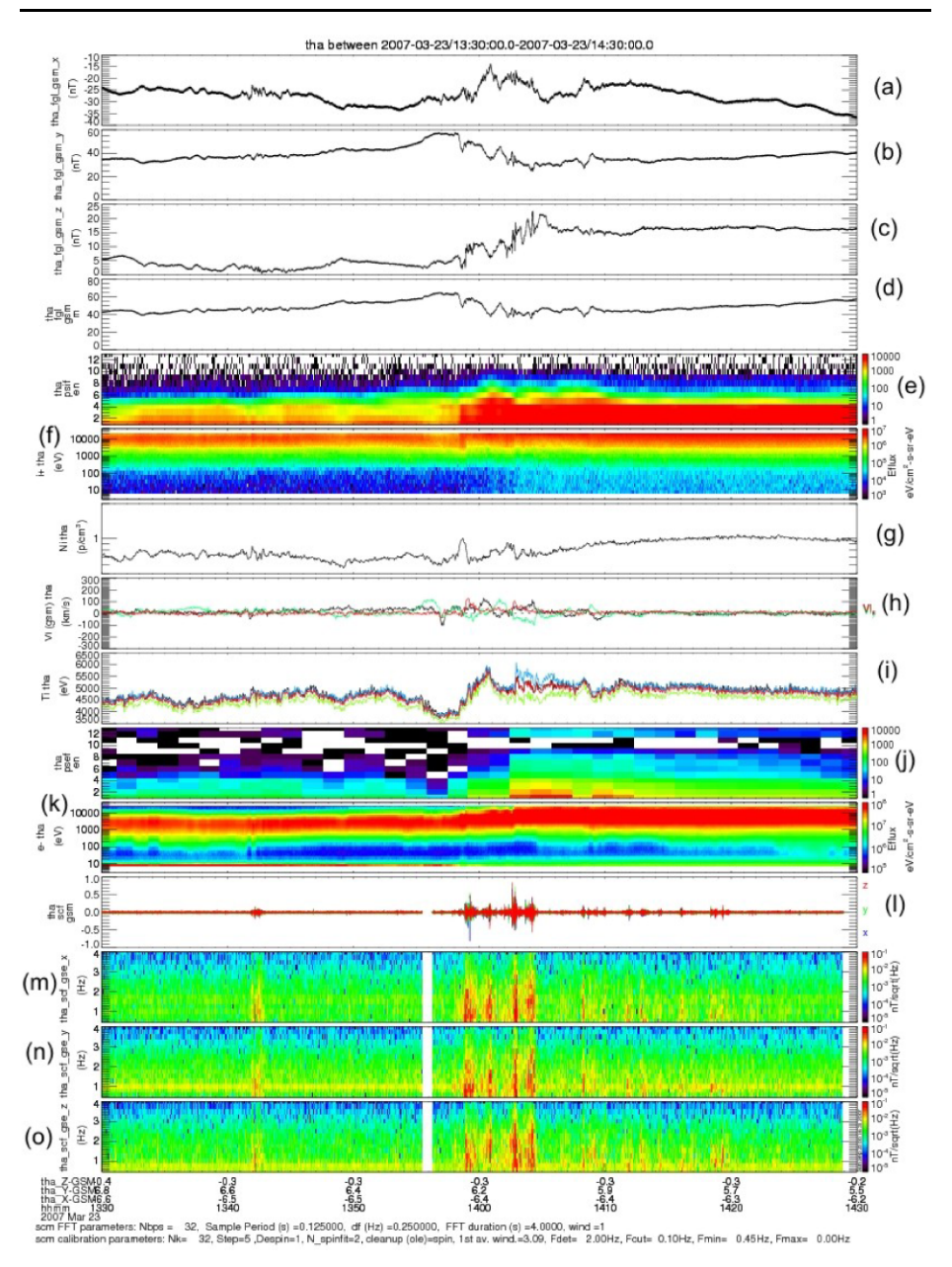


**Fig. 13** Overview of THA (fast survey) data on march 23rd 2007 between 1330 and 1430 UT. From *top* to *bottom:* Bx, By, Bz and B (FGM data), ion energy spectrograms (SST and ESA data), density, velocity and temperature, electron energy spectra (SST and ESA data), waveform and spectrograms of magnetic fluctuations from 0.45 Hz to 4 Hz (SCM data)

Le Contel et al. 2001b). They are poorly correlated with the velocity profiles shown in the next panels as compared with the first dipolarization. It could be due to the fact that all probes are farther from the source of the waves. The last panels (h, i, j) show the three



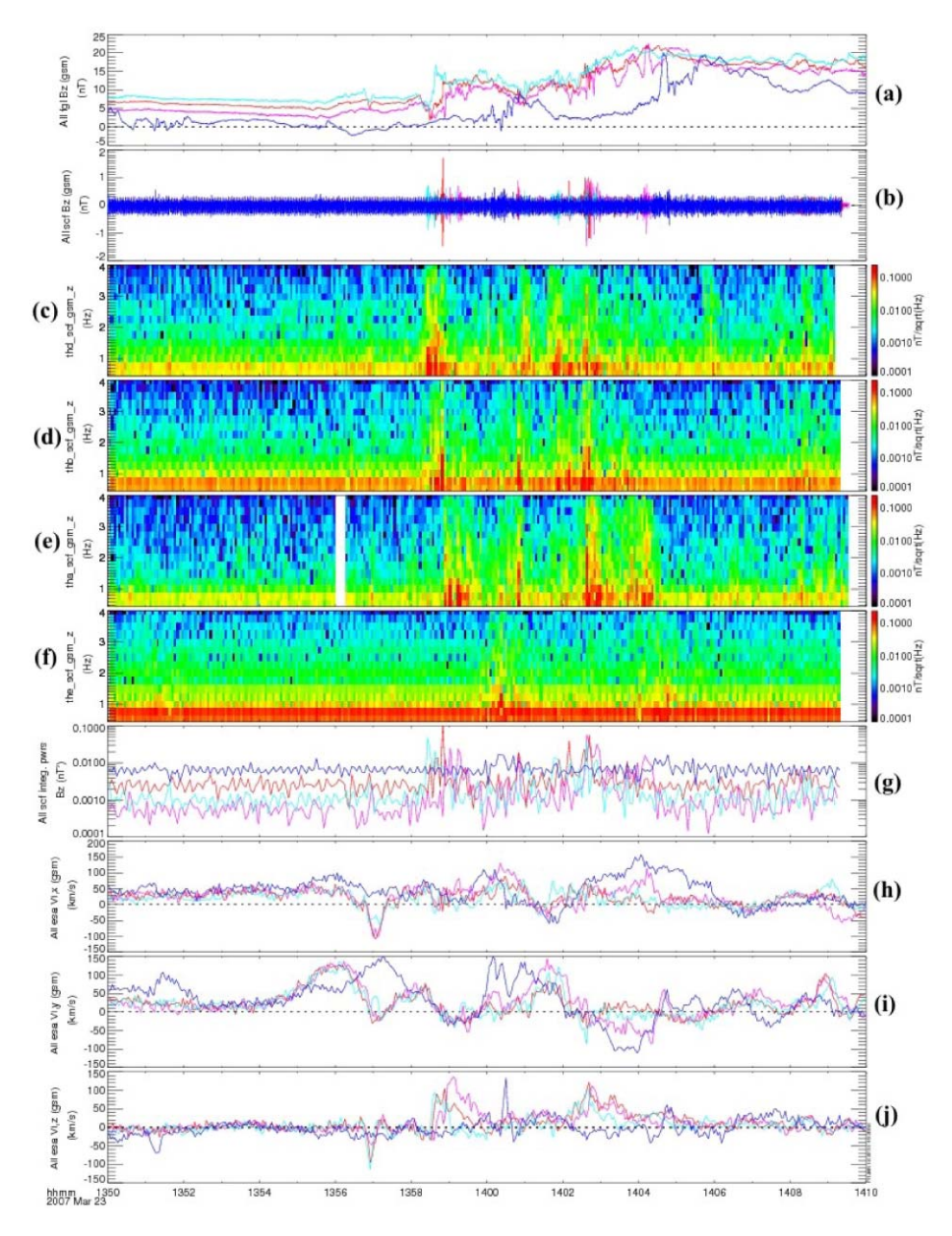


**Fig. 14** Data from four THEMIS probes  $(\mathbf{a}, \mathbf{b}, \mathbf{d}, \text{ and } \mathbf{e})$  in fast survey mode on March 23rd 2007 between 1350 and 1410 UT. Panel  $\mathbf{a}$ : Bz from FGM data with 0.5 s time resolution, panel  $\mathbf{b}$ : Bz from SCM data from 0.45 to 4 Hz, panels  $\mathbf{c}$  (THD),  $\mathbf{d}$  (THB),  $\mathbf{e}$  (THA),  $\mathbf{f}$  (THE): SCM Bz power spectral densities and panel  $\mathbf{g}$ : integrated powers from 0.45 to 4 Hz with 4 s time resolution, panels  $\mathbf{h}$ ,  $\mathbf{i}$ ,  $\mathbf{j}$ : x, y, and z components of the ion velocity with 3 s time resolution

components of the ion velocity. Amplitudes are smaller than for the first event. These lower velocities may be due to an underestimate of the velocities by ESA (see McFadden et al. 2008 for more details). Indeed the ion energy exceeds 40 keV, the upper energy limit of



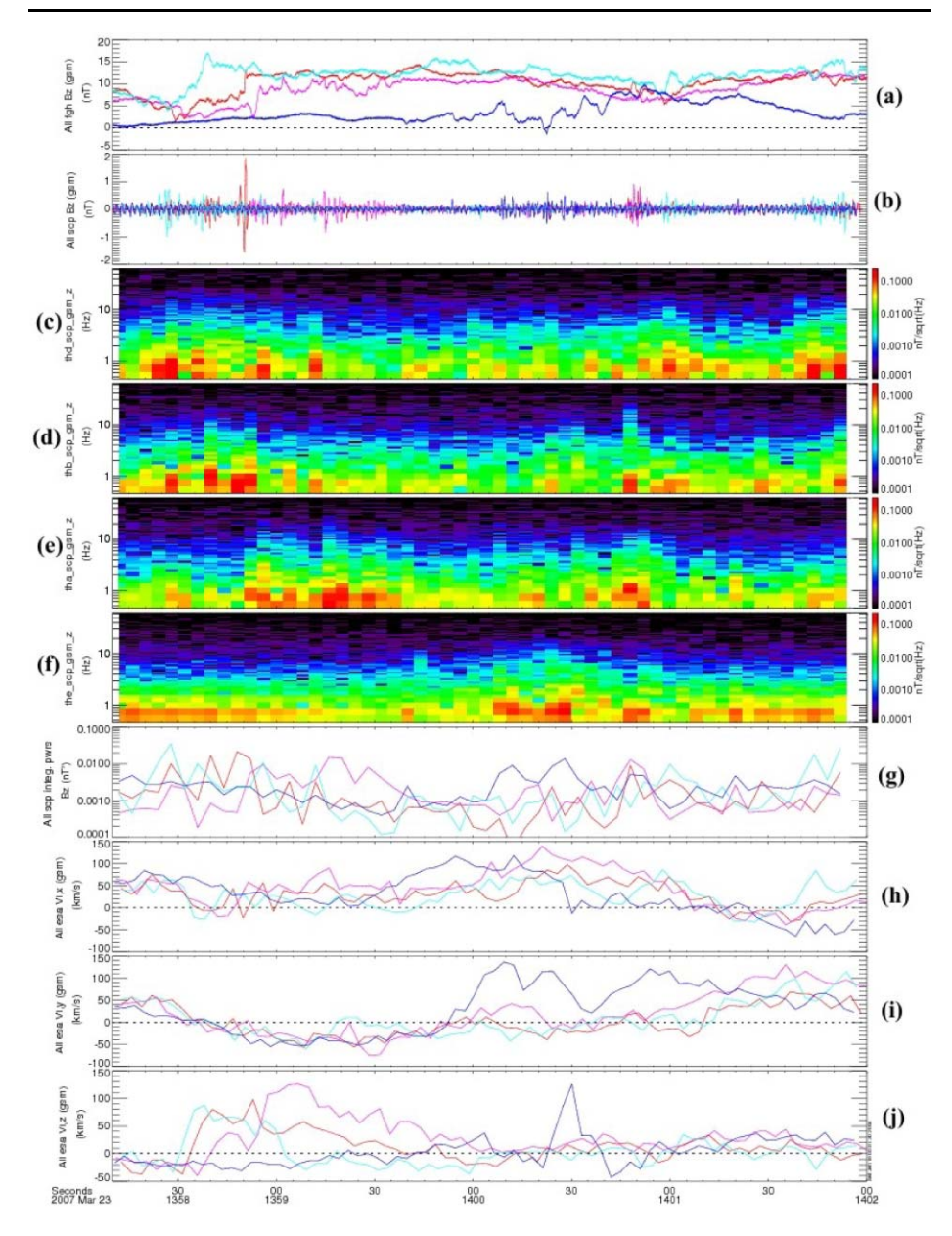


**Fig. 15** Four THEMIS probes (**a**, **b**, **d**, and **e**) data from particle burst mode on march 23rd 2007 between 1358:10 and 1402:00 UT. Panel **a**: Bz from FGM data sampled at 128 S/s, panel **b**: Bz from SCM data at 128 S/s filtered between 0.45 and 64 Hz, panels **c** (THD), **d** (THB), **e** (THA), **f** (THE): SCM Bz power spectral densities, and panel **g**: integrated powers from 0.45 to 64 Hz with 4 s of time resolution, panels **h**, **i**, **j**: x, y and z components of the ion velocity with 3 s of time resolution

ESA and clearly enters in the energy range of the SST instrument (see panels e and f on Fig. 13).



While the first dipolarization onset is characterized mainly by a large Vx component up to 350 km/s, the second one has a different signature: large values of the Vz component at the dipolarization onset (panel j). These large Vz values toward the magnetic equator are recorded in the same order as the dipolarization (THD, THB, and THA) and could be interpreted as the motion of the magnetic field lines toward the earth during the dipolarization. Figure 15 is the same as Fig. 14 but for the particle burst period during 1358:10 and 1402:00 UT. The time resolution is therefore better (FGM as well as SCM at 128 S/s). We observe the same signatures: dipolarization on THD, THB, THA and THE (panel a), ULF/ELF magnetic fluctuations up to 64 Hz but with maximum intensities still below 4 Hz (panels b, c, d, e and f), integrated power up to  $3 \times 10^{-2}$  (panel g), and large ion Vz at the dipolarization onset (panel j). Again the integrated power of magnetic fluctuations is somewhat smaller than previously reported values from geostationary spacecraft.

Note that no intense wave emission is recorded around  $f_{LH} \simeq 27$  Hz, the lower hybrid frequency which is well included in the range of the SCM. Finally we can remark that the SCM spectra performed from wave burst data shown in Fig. 3 are taken during this substorm period (135946–140016 UT). However the level of measured noise is similar to NEMI measured at ground. Therefore we can conclude that at least during this short lasting period no high-frequency waves are emitted notably in the range of whistler waves (between  $f_{c,i} \simeq 0.7$  Hz to  $f_{c,e} \simeq 1.4$  kHz).

# 5 Summary and Conclusions

The SCM and EFI are designed to characterize the electromagnetic fluctuations at substorm onset and to clarify their role in the different phases of the substorm expansion. We described the calibration method for the SCM instrument, as well as the spurious noise reduction process which recovers the sensitivity of the SCM instrument as it was measured on the ground.

First THEMIS SCM results, obtained in various regions, from the solar wind to the magnetotail, were presented and discussed. The usefulness of the magnetic fluctuations for the identification of the key regions of the magnetosphere was discussed, and their possible role in the different basic plasma processes was pointed out. Notably it was suggested that ULF fluctuations could heat electrons inside an FTE event (May 20, 2007). It has also been shown that the level of ULF magnetic fluctuations below 4 Hz (around  $f_{c,i}$ ) is largely enhanced during the substorm-related dipolarizations (March 23rd, 2007, 1113 and 1358 UT).

These first THEMIS SCM results demonstrate that the 5 tri-axis instruments function nominally, and illustrate the capability of the THEMIS mission to provide a comprehensive set of data not only on substorms but also on the physics of key regions such as the magnetopause and bow shock.

Acknowledgements We are pleased to acknowledge the friendly collaboration and the help of other THEMIS team members, in particular, P. Harvey, R. Jackson, J. Lewis, M. Ludlam, D. Meilhan, H. Richard, and E. Taylor. The French involvement on THEMIS is supported by CNES and CNRS. Work in the US was supported by NASA contract NAS5-02099. The work of KHG and UA at the Technical University of Braunschweig was financially supported by the German Ministerium für Wirtschaft und Technologie and the German Zentrum für Luft- und Raumfahrt under grant 50QP0402.

### References

V. Angelopoulos et al., Space Sci. Rev. (2008). doi:10.1007/s11214-008-9336-1



- N. Attico, F. Califano, F. Pegoraro, Phys. Plasmas 9, 458–464 (2002)
- H.U. Auster, K.H. Glassmeier, W. Magnes, O. Aydogar, W. Baumjohann, D. Constantinescu, D. Fischer, K.H. Fornacon, E. Georgescu, P. Harvey, O. Hillenmaier, R. Kroth, M. Ludlam, Y. Narita, R. Nakamura, K. Okrafka, F. Plaschke, I. Richter, H. Schwarzl, B. Stoll, A. Valavanoglou, M. Wiedemann, Space Sci. Rev. (2008). doi:10.1007/s11214-008-9365-9
- W. Baumjohann, A. Roux, O. Le Contel, R. Nakamura, J. Birm, M. Hoshino, A.T.Y. Lui, C.J. Owen, J.A. Sauvaud, A. Vaivads, D. Fontaine, A. Runov, Ann. Geophys. 25, 1365–1389 (2007)
- J. Bonnell et al., Space Sci. Rev. (2008 this issue)
- S.V. Bulanov, F. Pegoraro, A.S. Sakharov, Phys. Fluids B 4, 2499–2508 (1992)
- C.Z. Cheng, A.T.Y. Lui, Geophys. Res. Lett. 25, 4091 (1998)
- N. Cornilleau-Wehrlin, G. Chanteur, S. Perraut, L. Rezeau, P. Robert, A. Roux, C. Villedary, P. Canu, M. Maksimovic, Y. Conchy, D. Hubert, C. Lacombe, F. Lefeuvre, M. Parrot, J.-L. Pinçon, P.M.E. Décréau, C.C. Harvey, P. Louarn, O. Santolik, H.S. Alleyne, M. Roth, T. Chust, O. Le Contel, STAFF team, Ann. Geophys. 21, 437–456 (2003)
- R. Gendrin, Space Sci. Rev. 11, 54-130 (1970)
- D.A. Gurnett, L.A. Frank, R.P. Lepping, J. Geophys. Res. **81**, 6059–6071 (1976)
- V.I. Karpman, B.I. Meerson, A.B. Mikhailovsky, O.A. Pokholetov, Planet. Space Sci. 25, 273 (1977)
- V.V. Krasnosselskikh, B. Lembège, P. Savoini, V.V. Lobzin, Phys. Plasma 9, 1192–1209 (2003)
- G. Kremser, A. Korth, S.L. Ullaland, S. Perraut, A. Roux, A. Pedersen, R. Schmidt, P. Tanskanen, J. Geophys. Res. 93, 14,453 (1988)
- O. Le Contel, S. Perraut, A. Roux, R. Pellat, Space Sci. Rev. 95, 415–426 (2001a)
- O. Le Contel, A. Roux, S. Perraut, R. Pellat, Ø. Holter, A. Pedersen, A. Korth, J. Geophys. Res. 106, 10,817–10,827 (2001b)
- O. Le Contel, A. Roux, S. Perraut, R. Pellat, P. Robert, G. Chanteur, D. Fontaine, N. Cornilleau-Wehrlin, J.A. Sauvaud, C. Cully, G. Parks, D. Chua, M. André, A. Balogh, A. Fazakerley, H. Rème, T. Nagai, T. Mukai, H. Hayakawa, A. Matsuoka, R.R. Anderson, H. Matsumoto, in *Sixth International Conference on Substorms (ICS-6)*, ed. by R. Winglee. University of Washington, Seattle, 25–29 March 2002, pp. 326–333
- O. Le Contel, F. Sahraoui, A. Roux, D. Fontaine, P. Robert, J.A. Sauvaud, C. Owen, A.N. Fazakerley, in Eighth International Conference on Substorms (ICS-8), ed. by M. Syrjaeso, E. Donovan. University of Calgary, Canada, 27–31 March 2006, pp. 143–148
- M. Ludlam et al., Space Sci. Rev. (2008 this issue)
- A.T. Lui, R.E. Lopez, B.J. Anderson, K. Takahashi, L.J. Zanetti, R.W. McEntire, T.A. Potemra, D.M. Klumpar, E.M. Greene, R. Strangeway, J. Geophys. Res. 101, 13,067–13,088 (1996)
- A.T.Y. Lui, Rev. Geophys. **39**(4), 535–563 (2001)
- A.T.Y. Lui, C.L. Chang, A. Mankofsky, H.K. Wong, D. Winske, J. Geophys. Res. 96, 11,389–11,401 (1991)
- M.E. Mandt, R.E. Denton, J.F. Drake, Geophys. Res. Lett. **21**(1), 73–77 (1994)
- J.P. McFadden, C.W. Carlson, D. Larson, V. Angelopoulos, Space Sci. Rev. (2008 this issue)
- S. Perraut, O. Le Contel, A. Roux, A. Pedersen, J. Geophys. Res. 105, 21,097–21,107 (2000a)
- S. Perraut, O. Le Contel, A. Roux, R. Pellat, A. Korth, Ø. Holter, A. Pedersen, Geophys. Res. Lett. 4041–4044 (2000b)
- S. Perraut, A. Morane, A. Roux, A. Pedersen, R. Schmidt, A. Korth, G. Kremser, B. Aparicio, R. Pellinen, Adv. Space Res. 13(4), 217 (1993)
- T. Quinn, J.W. Bonnell, A. Roux, U. Auster, D. Larson, K. Khurana, M. Ludlam, P. Harvey, V. Angelopoulos, THEMIS Science Coordinate Systems Definition THM-SOC-110, 29 September 2006
- L. Rezeau, G. Belmont, Space Sci. Rev. 95, 427–441 (2001)
- P. Robert, R. Gendrin, S. Perraut, A. Roux, A. Pedersen, J. Geophys. Res. 89, 819 (1984)
- A. Roux, O. Le Contel, P. Robert, C. Coillot, A. Bouabdellah, B. la Porte, D. Alison, S. Ruocco, M.C. Vassal, Space Sci. Rev. (2008 this issue)
- C.T. Russel, Planet. Space Sci. **20**, 1541–1553 (1972)
- F. Sahraoui, J.L. Pinçon, G. Belmont, L. Rezeau, N. Cornilleau-Wehrlin, P. Robert, L. Mellul, J.M. Bosqued, A. Balogh, P. Canu, G. Chanteur, J. Geophys. Res. 108, 1335 (2003). doi:10.1029/2002JA009587
- I. Shinohara, T. Nagai, M. Fujimoto, T. Terasawa, T. Mikai, K. Tsuruda, T. Yamamoto, J. Geophys. Res. 103, 20,365 (1998)
- K. Shiokawa, Y. Miyashita, I. Shinohara, A. Matsuoka, J. Geophys. Res. 110, 219 (2005). doi:10.1029/ 2005JA011144
- D.G. Sibeck, V. Angelopoulos, Space Sci. Rev. (2008a this issue)
- D.G. Sibeck et al., Geophys. Res. Lett. (2008b). doi:10.1029/2008GL033568
- K. Sigsbee, C.A. Cattell, F.S. Mozer, K. Tsuruda, S. Kokubun, J. Geophys. Res. 106, 435–445 (2001)
- Y. Zhang, H. Matsumoto, H. Kojima, J. Geophys. Res. **104**, 28,633–28,644 (1999)

